

**Synthesis of  $V_2O_3$  nanoplates for the exploration of the correlated supercritical state**Hamid Reza Rasouli,<sup>1</sup> Naveed Mehmood,<sup>1</sup> Onur Çakıroğlu,<sup>2</sup> Engin Can Sürmeli,<sup>1</sup> and T. Serkan Kasırğa<sup>1,2,\*</sup><sup>1</sup>*Bilkent University UNAM, National Nanotechnology Research Center, Ankara, Turkey 06800*<sup>2</sup>*Department of Physics, Bilkent University, Ankara, Turkey 06800*

(Received 5 August 2019; revised manuscript received 8 October 2019; published 21 October 2019)

Peculiar features exist in the stress-temperature phase stability diagram of  $V_2O_3$ , such as a first-order phase transition between the paramagnetic insulating and metallic phases that ends with a critical point, quantum phase transition, and a triple point. These features remain largely unexplored, and the exact nature of the phase transitions is not clear due to very limited control over the stress in bulk or film samples. Here, we show the synthesis of single-crystal  $V_2O_3$  nanoplates using chemical vapor deposition via van der Waals epitaxy. Thickness of the  $V_2O_3$  nanoplates range from a few to hundreds of nanometers, and they can be mechanically exfoliated from the growth substrate. Using Raman spectroscopy on the nanoplates, we reveal that, upon heating,  $V_2O_3$  enters a supercritical state for both tensile strained and relaxed crystals with a similar out-of-plane response. Transmission electron microscopy on  $V_2O_3$  nanoplates hints at the existence of a structural change when the crystals are heated. Our results show that  $V_2O_3$  nanoplates should be useful for studying the physics of the supercritical state and the phase stability of  $V_2O_3$  to enable new horizons in applications.

DOI: [10.1103/PhysRevB.100.161107](https://doi.org/10.1103/PhysRevB.100.161107)

Vanadium oxides display peculiar properties due to the unpaired  $d$  electrons in vanadium's valance. Interplay among the internal degrees of freedom, such as spin, charge, and orbital leads to rich electronic phenomena, such as metal-insulator transition (MIT) [1], unusual quantum spin states [2,3], and superconductivity [4]. These phenomena are remarkably sensitive to the external stimuli, such as temperature, stress, and doping in vanadium oxides. Thus, studying them in bulk or film samples results in multiple problems, such as various phase and domain formations due to nonuniform strain and compositional variations due to local doping and oxygen vacancies [5,6]. These problems can be avoided by the use of crystals that are smaller than the characteristic domain size [7–9]. Free-standing  $VO_2$  nanocrystals, for instance, have been used to determine the metal-insulator phase stability diagram and led to the observation of a solid-state triple point [10].

At the room temperature,  $V_2O_3$  is in the paramagnetic metallic (PM) corundum phase, whereas, at about 160 K, it turns into the antiferromagnetic insulating (AFI) monoclinic phase [1,11]. Furthermore, tensile stress stabilizes the paramagnetic-insulating (PI) corundum phase at room temperature or above [12]. Besides the first-order phase transitions, when the crystal is under tensile stress at elevated temperatures ( $\sim 400$  K), PI and PM phase equilibria ends with the solid-state critical point to enter a solid-state supercritical state analogous to supercritical fluids. A depiction of the stress-temperature phase stability diagram of  $V_2O_3$  is given in Fig. 1(a) [11]. Attempts to explore the MITs and the criticality in  $V_2O_3$  have been mainly focused on chromium-doped samples as PI to PM transition can be obtained without tensile straining the crystal [12–15]. When  $V_2O_3$  is doped

by a certain amount of Cr, the PI phase becomes stable in unstrained crystals. However, this simple minded approach leads to poor metallicity [15] due to coexistence of the metallic and insulating domains stabilized by structural defects [16]. Furthermore, the MIT is shown to be inequivalent to the one observed via application of compressive stress [17–19]. Further complications arise in film samples due to polycrystallinity of the films and nonuniform stress due to the substrate adhesion as well as lattice mismatch-induced stresses in epitaxially grown films. Similarly, bulk crystals of  $V_2O_3$  present other challenges, such as irreproducibility in measured quantities [20,21]. So far, no free-standing high-quality crystals smaller than the characteristic domain size were available for  $V_2O_3$  due to the difficulties in the synthesis. Thus, the tremendous potential to study the criticality of the Mott transition has not been fully realized [14], and the precise details of the phase diagram are still unclear [22]. In this Rapid Communication, we show a route to synthesize high-quality layered  $V_2O_3$  single crystals of a few nanometer thickness and study some novel aspects of the phase transitions.

Our crystal synthesis method relies on salt-assisted chemical vapor deposition of nanoplates. Potassium iodide (KI) salt is reacted with  $V_2O_5$  at an elevated temperature to form potassium vanadate [23], an intermediate compound that can be further reduced to  $V_2O_3$  with  $H_2$ . This chemical route results in much higher-quality crystals as compared to the direct reduction of  $V_2O_5$  via  $H_2$  and sulfur [24] or a reduction of  $V_2O_5$  in molten potassium fluoride [25]. Our synthesis takes place in a custom-made chemical vapor deposition chamber we reported earlier, that allows real-time optical observation and control of the synthesis [26,27]. A series of optical microscope images taken during the growth given in Fig. 1(b) shows the formation of the crystals. Although real-time observation of the synthesis allowed us to determine the growth conditions leading to  $V_2O_3$  nanoplates and prepare

\*Corresponding author: [kasirga@unam.bilkent.edu.tr](mailto:kasirga@unam.bilkent.edu.tr)

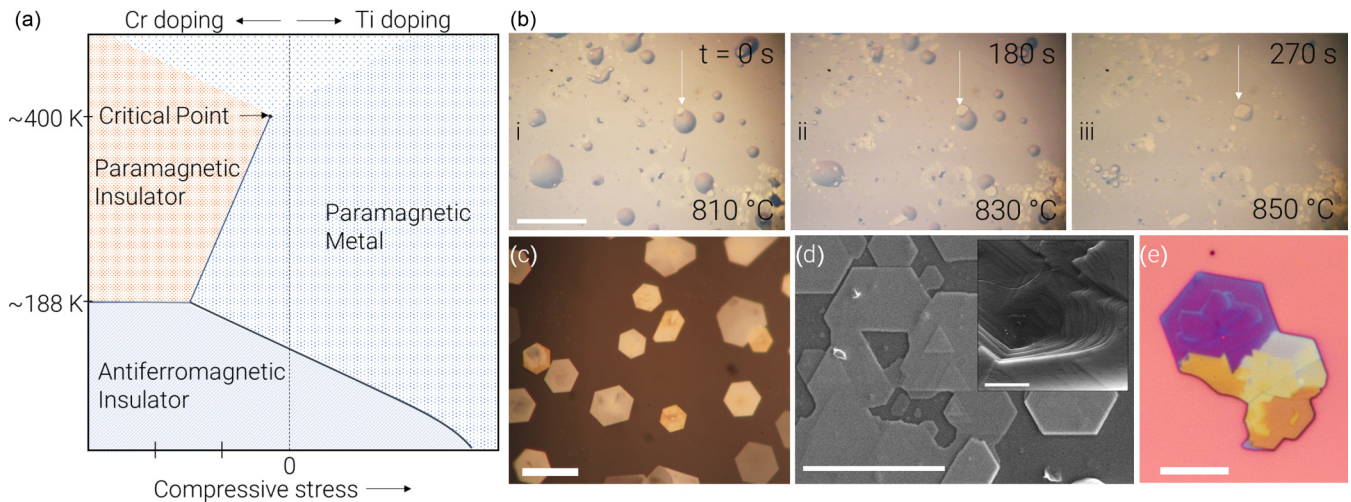


FIG. 1. (a) Tentative phase stability diagram of  $V_2O_3$  is depicted in the figure based on the previous reports. The effect of doping and stress is illustrated on the lateral axis, and the effect of the temperature is illustrated on the vertical axis. Marked temperatures on the graph designate the temperature of the critical point and the triple point. The shaded region above 400 K, beyond the critical point, depicts the supercritical state where Mott criticality is prevalent. Markings on the horizontal axis indicate 4-kbars/division hydrostatic pressure. (b) The optical microscope micrographs taken during the salt-assisted synthesis show the crystal formation stages. Images are taken from 810 °C to 850 °C, and the beginning of the observation in (i) is marked as time zero ( $t = 0$  s). As the time passes by (ii) and (iii), thin crystals nucleate from the liquid flux. The white arrow indicates an exemplary crystal formation. The scale bar is 50  $\mu\text{m}$ , and subsequent images share the same scale bar. (c) The optical microscope micrograph shows crystal formations of various thicknesses on sapphire. The scale bar is 20  $\mu\text{m}$ . (d) The scanning electron microscopy (SEM) micrograph shows layer-by-layer growth, and the inset is a closeup view of the edge of a crystal. The scale bars are 20  $\mu\text{m}$  for the main figure and 1  $\mu\text{m}$  for the inset. (e) The optical microscope micrograph of a  $V_2O_3$  nanoplate transferred on to an oxidized Si chip showing the crystal mechanically exfoliated from the substrate. The scale bar is 10  $\mu\text{m}$ .

the growth recipes, any conventional split tube furnace can be used for the nanoplate synthesis.

Optical microscope micrographs show crystals of varying thicknesses [Fig. 1(c)]. Images obtained by SEM given in Fig. 1(d) and in its inset reveal layer-by-layer growth of the crystals. This mechanism is commonly observed in the crystal formation from supersaturated liquid precursors [28]. As the solute particles energetically favor to attach to kinks rather than flat surfaces, such steps occur. Strikingly, these layers can be exfoliated mechanically. When we transfer crystals from the growth substrate onto the  $\text{SiO}_2/\text{Si}$  substrate using cellulose acetate butyrate, transferred crystals typically have a few nanometer thin layers attached to the thicker crystals [29]. An example is shown in Fig. 1(e). Such exfoliation from the bulk is observed in both van der Waals stacked two-dimensional (2D) layered materials and non-van der Waals stacked materials: Hematite, which shares the same crystal structure with the metallic phase of  $V_2O_3$ , and ilmenite 2D layers have been obtained via liquid phase exfoliation [30,31]. Atomic force microscope (AFM) scans show that the minimum step height among the layers is 0.6 nm [27].

To confirm the chemical composition of the synthesized crystals, we performed wavelength dispersive x-ray spectroscopy (WDS) and x-ray photoelectron spectroscopy (XPS). WDS spectra taken from a few tens of nanometer thick crystals show only V and O in the crystals. Consistent with the WDS, XPS surveys show that there are O, V, and Al yet no I and K for the samples when rinsed with de-ionized water [27,32–35]. X-ray diffraction (XRD) confirms the  $c$  axis of the sapphire substrate and the synthesized crystals are parallel to each other [27,36,37]. We consider that nanoplate growth on

the sapphire surface to be an incommensurate van der Waals epitaxy [38]. Lattice mismatch between the  $c$ -cut sapphire and  $V_2O_3$  would result in 4.1% biaxial in-plane tensile strain. However, as we discuss in the following paragraph, this level of strain is unlikely [39]. We would like to emphasize one more time that  $V_2O_3$  crystals can be mechanically removed from the substrate surface. Another observation that supports the incommensurate van der Waals epitaxy is our failed attempts to grow  $V_2O_3$  crystals on various substrates, such as oxidized Si, Si, and quartz.

Raman spectrum of paramagnetic (PM)  $V_2O_3$  has been reported to have six well-defined peaks corresponding to  $E_g$  and  $A_{1g}$  vibrational modes at 203, 290, 590, 231, and 500  $\text{cm}^{-1}$ , respectively [40,41]. Raman spectra for our as-grown crystals on sapphire have peaks around 248, 305, 514, and 590  $\text{cm}^{-1}$ , and they match well with the spectrum of the paramagnetic-insulating phase reported by Tatsuyama and Fan for  $(V_{0.985}Cr_{0.015})_2O_3$  (see Table S1 in the Supplemental Material [27] for a detailed comparison of our measurements with the literature) [41]. Due to the thermal expansion coefficient (TEC) difference between sapphire and  $V_2O_3$ , when the crystals cooled down to the room temperature, they are under tensile stress [42]. Indeed, from the temperature where crystals form ( $\sim 850$  °C) down to room temperature, TEC difference perpendicular to the corundum  $c$  axis accounts for  $\sim 1.1\%$  tensile strain on the crystals [27,43,44]. This corresponds to 0.29% volumetric expansion or  $-6.6$ -kbars equivalent hydrostatic pressure [12]. In the phase stability diagram of McWhan *et al.* [11], such negative pressure is enough to stabilize the PI phase at room temperature. This shows the equivalence of the in-plane strain to the hydrostatic

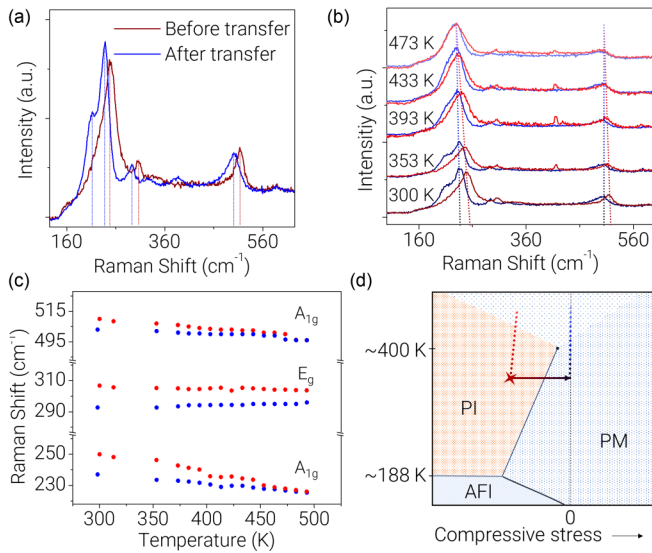


FIG. 2. (a) Raman spectra of as-grown and transferred  $V_2O_3$  on sapphire are given in the figure. Major Raman modes reported in the literature are marked by dashed lines with respective colors. (b) Raman spectra of as-grown (red series) and transferred (blue series) crystals become similar upon heating. The  $E_g$  mode around  $210\text{ cm}^{-1}$  gradually disappears with the increasing temperature, and the  $A_{1g}$  mode softens in both cases to merge around  $450\text{ K}$ . The peak around  $416\text{ cm}^{-1}$  is due to the sapphire substrate. (c) Temperature dependences of the peak Raman modes for as-grown (red points) and transferred (blue points) crystals are given in the figure. Raman peak positions can be determined with  $\pm 0.5\text{-cm}^{-1}$  precision. (d) Effects of releasing the crystals and heating both as-grown and transferred crystals are illustrated on the tentative phase stability diagram. The red star marks the tentative stress on the as-grown nanoplate at room temperature, and the solid arrow emerging from it indicates the effect of transferring. The red and blue dotted lines depict how both as-grown and transferred crystals, respectively, enter the supercritical state. The red dotted line is drawn slanted as the temperature increase will reduce the tensile stress due to differences in thermal expansions of  $V_2O_3$  and the substrate.

pressure. The mismatch between TECs also implies that the growth temperature has an influence on the strain at room temperature. Lower growth temperature will result in larger effective hydrostatic pressure. As we discuss in the following paragraphs, these observations are consistent with the fact that as-synthesized crystals are in the paramagnetic-insulating phase.

A striking change takes place in the Raman spectrum after releasing crystals from the sapphire surface or when the crystals are agitated strongly on the sapphire surface. Figure 2(a) shows the Raman spectrum of a crystal transferred [27] onto a clean sapphire substrate and a crystal on the growth substrate for comparison. Peak positions of the transferred crystals match very well with those of the PM phase reported earlier [27,40,41]. This change in the spectrum can be explained by the phase transition from the PI to the PM phase due to the relaxation of the tensile stress on the crystals.

When we heat  $V_2O_3$  thin crystals, we observe reversible softening of the Raman modes especially above  $400\text{ K}$  [Fig. 2(b)]. Intriguingly, crystals both as-grown and

transferred to a pristine substrate show the similar Raman features above  $400\text{ K}$ . Cooling back to room temperature retrieves the initial spectra for both phases. This observation can be explained by emergence of the supercritical state upon heating  $V_2O_3$ . As the PI and PM phase boundaries end in a second-order critical end point [14], crystals heated into the supercritical state display a unique Raman spectra irrespective of their initial phase. Figure 2(c) shows the temperature dependence of Raman peaks that persists up to the supercritical state for both PI and PM crystals.  $A_{1g}$  peaks for both PI and PM phases merge at elevated temperatures whereas the  $E_g$  peaks show little variation with the temperature. This observation can be explained by insensitivity of in-plane  $E_g$  modes to the second-order phase transition since the  $e_g(\pi)$  band is perpendicular to the  $c$  axis [45] and the motion of atoms along the  $c$  axis mainly affects the  $A_{1g}$  modes [41]. Figure 2(d) depicts how different initial phases end up in similar Raman responses on a tentative phase stability diagram. This point is also supported by the asymmetry observed in the  $514\text{-cm}^{-1}$  peak at the supercritical state. The asymmetric feature can be attributed to the Fano resonances of Raman active electronic transitions across  $a_{1g}$  and  $e_g(\pi)$  bands near the Fermi level [46]. As the number of electrons in the  $a_{1g}$  band increases in the supercritical state compared to the PI phase, the continuum electronic Raman process belonging to the same symmetry group as the phonon Raman scattering due to  $A_{1g}$  phonons may interact with each other. Interaction between a discrete process with a continuum process results in an asymmetry in the Raman peak.

To further characterize the crystal structure and crystallinity of the nanoplates, we performed transmission electron microscopy (TEM) and selected area electron diffraction (SAED) on  $V_2O_3$  nanoplates transferred to holey carbon and silicon nitride TEM grids [Figs. 3(a)–3(d)]. We also took high-resolution TEM images and SAED patterns from the cross section of the  $V_2O_3$  on sapphire [Figs. 3(e) and 3(f)]. When the zone axis is perpendicular to the sample surface, we find a sixfold symmetric arrangement with  $d$  spacing of  $2.5\text{ \AA}$  for the  $(10\bar{1}0)$  plane. This is consistent with the XRD measurements as the corundum  $c$  axis points perpendicular to the nanoplate surface. However, the SAED pattern taken along different zone axes match exactly with a face-centered-cubic (fcc) structure rather than more commonly reported hexagonal-closed-packed (hcp) corundum structure. Figures 3(b)–3(d) show SAED patterns taken through various zone axes, and angles between various planes are measured. This measurement is confirmed in five separate crystals transferred via different methods.

The most plausible explanation for the observed shift in stacking from hcp to fcc is a slight structural change upon heating of the crystals by the electron beam to the supercritical state. A temperature rise of  $\sim 150\text{ K}$  is sufficient for emergence of the supercritical state in the nanoplates. Indeed, as the crystals are suspended on the TEM grid with minimal thermal contact with the environment, we measure a temperature increase of up to  $\sim 4\text{ K}$  per microwatt of laser power in Raman spectroscopy [27]. In a recent study, electron-beam heating in TEM is measured using the MIT in  $VO_2$  nanocrystals, and even with very modest electron flux, it is possible to induce a significant temperature rise in the

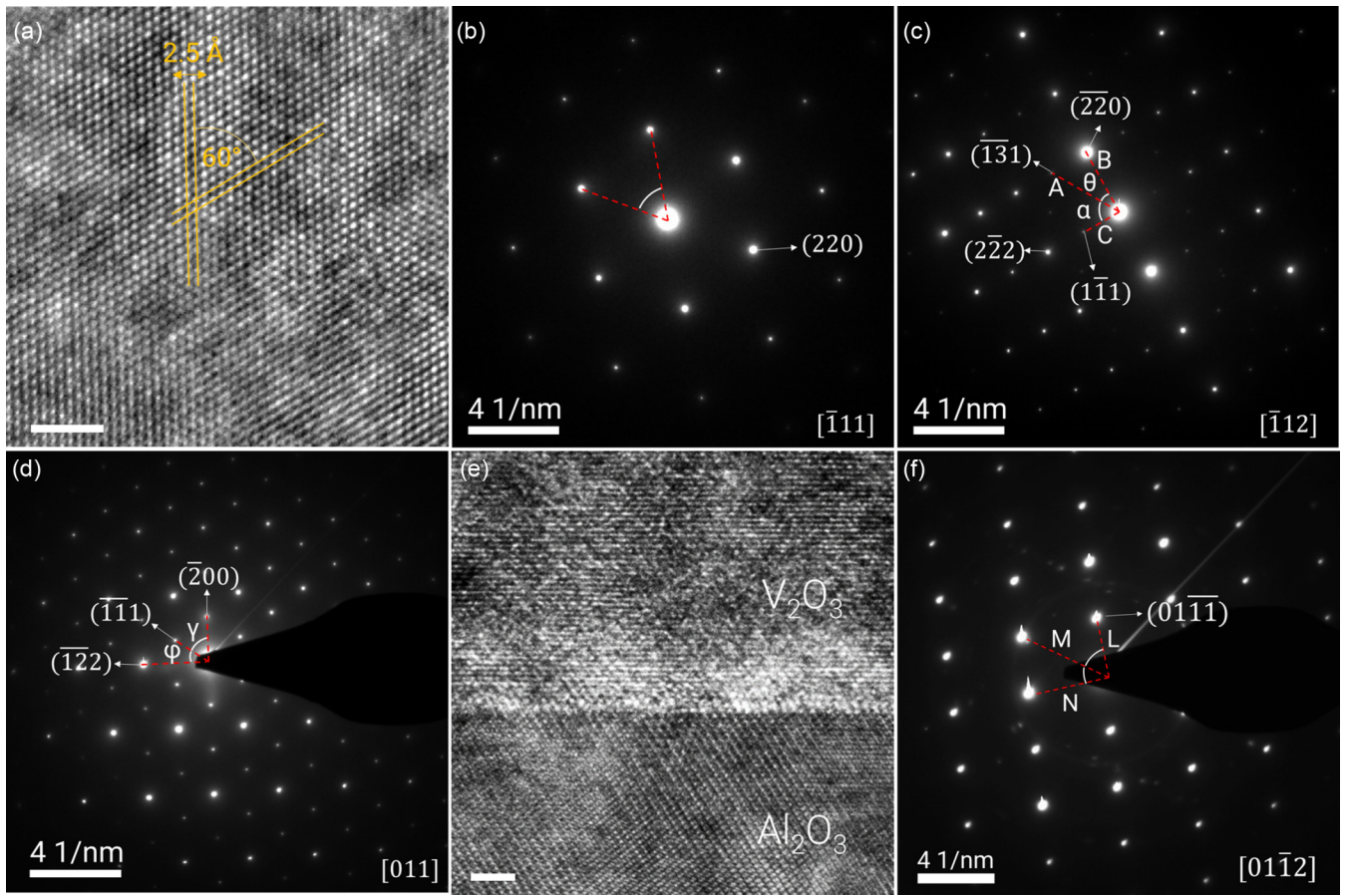


FIG. 3. (a) High-resolution- (HR-) TEM image of a  $V_2O_3$  crystal. The close-packed structure is evident. The scale bar is 2 nm. (b) Sixfold symmetric SAED pattern indexed according to the fcc  $[\bar{1}11]$  direction. However, the same pattern is produced for the hcp  $[0001]$  direction. The lengths of the red dashed lines are  $4 \text{ nm}^{-1}$ , corresponding to  $2.5\text{-}\text{\AA}$   $d$  spacing along  $(220)$  fcc or  $(10\bar{1}0)$  hcp planes. (c) Once the sample is tilted to a different zone axis, the difference between the fcc and the hcp structures becomes clear. No such pattern can be found for hcp. The angles between the principal plane normals  $\theta = 39.23^\circ$ ,  $\alpha = 50.77^\circ$ , and the ratios of the principal spot spacings  $B/C = 1.633$ ,  $A/C = 1.915$  match exactly with the standard indexed diffraction pattern for fcc crystals. (d) Another specific fcc diffraction pattern is obtained and indexed along the  $[011]$  direction. The angles between the principal plane normals  $\gamma = 54.74^\circ$  and  $\phi = 35.26^\circ$  matches perfectly with the standard indexed diffraction pattern for fcc crystals. (e) The cross-sectional HR-TEM image shows the stacking of the  $V_2O_3$  crystal on the  $Al_2O_3$  substrate. The scale bar is 2 nm. (f) SAED pattern taken from the  $V_2O_3$  sample prepared for the cross-sectional TEM imaging can be uniquely indexed with the hcp  $[01\bar{1}2]$  diffraction pattern. Both angles between the principal plane normals and  $N/L = 1.52$  and  $M/L = 1.82$  match very well with the standard indexed SAED for hcp.

cantilevered nanocrystals [47]. Other evidence that supports the electron-beam-induced heating to cause the structural change is from the SAED pattern taken from the cross-sectional TEM samples [Figs. 3(e) and 3(f)]. As the  $V_2O_3$  crystal is sandwiched between the sapphire substrate and the platinum top layer, it is not thermally insulated from the support structures. Thus, we claim that the beam-induced heating in this case is not high enough to cause the hcp to fcc transition. The SAED pattern taken from the cross-sectional sample matches very well with the hcp corundum structure [Fig. 3(f)]. We would like to note that there are no previous reports of a fcc structure for the high-temperature  $V_2O_3$  and further studies are required to elaborate this intriguing observation. In parallel with our Raman and SAED measurements, an anomalous increase in the resistivity of the PM phase [20,48] and a minimum in the  $c$ -axis lattice parameter [42] around 400 K are observed.

Now, we turn our attention to the electrical properties of the nanoplates. Resistance vs temperature (RT) curve taken on as-grown crystals using a four-terminal configuration from 150 to 300 K shows activated electrical conduction throughout the entire temperature regime with a rapid increase in the resistivity below 188 K [Fig. 4(a)]. This is consistent with the fact that our as-grown crystals are in the PI phase, and as they cool down, PI to AFI transition takes place at the previously reported transition temperature [11]. Phase transition is not sharp since as-grown crystals are under nonuniform stress due to the surface adhesion leading to the coexistence of PI and AFI phases over a temperature range. Resistivity  $[\rho(T)]$  vs temperature ( $T$ ) curve below 188 K, except the vicinity of the phase-transition temperature, can be fitted with an Arrhenius relation  $\rho(T) = \rho_0 c^{E_A/k_B T}$  with  $E_A = 0.195 \pm 0.005$  eV as the activation energy,  $k_B$  is Boltzmann's constant, and  $\rho_0$  is a constant [20].

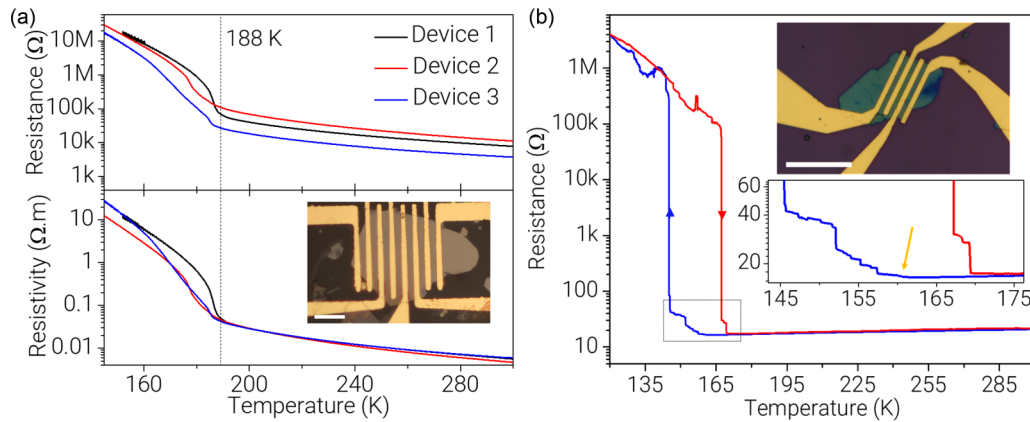


FIG. 4. (a) Resistance and resistivity vs temperature curves for three different devices are given in the graph. All devices show insulator-to-metal transition around 188 K. The inset in the lower panel shows a typical as-grown nanoplate patterned using optical lithography. The scale bar is  $20 \mu\text{m}$ . (b) Resistance vs temperature curve for a transferred  $V_2O_3$  crystal. For this particular sample, there is a  $5\frac{1}{2}$  orders of magnitude change in the resistivity. Here, blue and red colors represent cooling and heating, respectively. The lower inset shows a scale up of the region marked with a dashed rectangle. The onset of the phase transition is around 160 K. The upper inset shows a typical device patterned using electron-beam lithography.

When we transfer the nanoplates from the growth substrate to an oxidized Si chip, tensile stress on the nanoplate is released, and the nanoplate turns to the PM phase. We observe the metallic resistivity down to  $\sim 160$  K [Fig. 4(b)]. At 160 K, MIT begins. MIT is not abrupt in our devices since the nanoplate still adheres to the  $\text{SiO}_2$  surface. Moreover, due to the clamping effect of the electrical contacts, some force is exerted on the nanoplate upon the onset of phase transition since the in-plane lattice constant increases significantly during the MIT. This results in a coexistence of the metallic and the insulating phases over a temperature range and produce a staircaselike change in the resistance with the temperature [49]. Based on the RT measurements with known crystal thicknesses, we calculated the temperature-dependent resistivity [ $\rho(T)$ ] of the metallic phase as  $\rho(T)/\rho(273 \text{ K}) = 0.58 + 1.5 \times 10^{-3}T$ .  $\rho(T)/\rho(273 \text{ K})$  is comparable to the bulk samples [48,50].

High-quality  $V_2O_3$  nanoplates that we introduce in this Rapid Communication can be both tensile and compressively stressed. As we demonstrated, this in-plane stress is equivalent to the hydrostatic pressure and may provide a unique opportunity to study the phase stability diagram of pure  $V_2O_3$ . In particular, these crystals may enable a detailed study of the supercritical state and crossover along the Widom line [51] that separates the Mott insulator-like and correlated metal-like regions. As we illustrated in this Rapid Communication,  $A_{1g}$  Raman-active phonon modes become indistinguishable when heated to the supercritical region whereas  $E_{1g}$  modes retain their initial phase characteristics. Thus, mapping of the Raman

peaks within the supercritical region via controlling the in-plane strain may reveal the universality of this observation in the light of the recent advances in the understanding of the Widom line theoretically [52] and experimentally [53,54] in fundamentally different systems. The fcc structure we observed under electron-beam imaging requires further investigation as the existence of various phases may provide further insight towards theoretical understanding of the supercritical state. Furthermore, our crystals can be thinned down to a few nanometers in thickness under an inert atmosphere. This may enable the study of MIT in a 2D system, and these crystals would be a very suitable test platform for the field-effect experiments on various regions of the phase diagram [55]. These correlated nanoplates can be used in the study of van der Waals-like novel heterostructures for reconfigurable electronics and optoelectronics [56–58].

This work was supported by the Scientific and Technological Research Council of Turkey (TUBITAK) under Grant No. 116M226. The authors thank D. H. Cobden for useful discussions.

T.S.K. conceived the project. H.R.R. and T.S.K. performed the experiments. N.M. and E.C.S. helped with device fabrication and Raman measurements. N.M. performed the crystal transfers. O.Ç. performed the AFM measurements. The Rapid Communication was written with contributions from all authors. All authors have given approval for the final version of the Rapid Communication.

The authors declare no competing financial interests.

- [1] F. J. Morin, *Phys. Rev. Lett.* **3**, 34 (1959).  
 [2] H. Harashina, K. Kodama, S. Shamoto, S. Taniguchi, T. Nishikawa, M. Sato, K. Kakurai, and M. Nishi, *J. Phys. Soc. Japan* **65**, 1570 (1996).  
 [3] L. Krusin-Elbaum, D. M. Newns, H. Zeng, V. Derycke, J. Z. Sun, and R. Sandstrom, *Nature (London)* **431**, 672 (2004).

- [4] T. Yamauchi, Y. Ueda, and N. Mōri, *Phys. Rev. Lett.* **89**, 057002 (2002).  
 [5] E. Dagotto, *Science* **309**, 257 (2005).  
 [6] A. Pustogow, A. S. McLeod, Y. Saito, D. N. Basov, and M. Dressel, *Sci. Adv.* **4**, eaau9123 (2018).

- [7] B. S. Guiton, Q. Gu, A. L. Prieto, M. S. Gudiksen, and H. Park, *J. Am. Chem. Soc.* **127**, 498 (2005).
- [8] J. Wei, Z. Wang, W. Chen, and D. H. Cobden, *Nat. Nanotechnol.* **4**, 420 (2009).
- [9] V. N. Andreev, F. A. Chudnovskiy, J. M. Honig, and P. A. Metcalf, *Phys. Rev. B* **70**, 235124 (2004).
- [10] J. H. Park, J. M. Coy, T. S. Kasirga, C. Huang, Z. Fei, S. Hunter, and D. H. Cobden, *Nature (London)* **500**, 431 (2013).
- [11] D. B. McWhan, A. Menth, J. P. Remeika, W. F. Brinkman, and T. M. Rice, *Phys. Rev. B* **7**, 1920 (1973).
- [12] D. B. McWhan and J. P. Remeika, *Phys. Rev. B* **2**, 3734 (1970).
- [13] H. Yang and R. J. Sladek, *Phys. Rev. B* **32**, 6634 (1985).
- [14] P. Limelette, A. Georges, D. Jerome, P. Wzietek, P. Metcalf, and J. M. Honig, *Science* **302**, 89 (2003).
- [15] S. Lupi, L. Baldassarre, B. Mansart, A. Perucchi, A. Barinov, P. Dudin, E. Papalazarou, F. Rodolakis, J. P. Rueff, J. P. Itié, S. Ravy, D. Nicoletti, P. Postorino, P. Hansmann, N. Parragh, A. Toschi, T. Saha-Dasgupta, O. K. Andersen, G. Sangiovanni, K. Held, and M. Marsi, *Nat. Commun.* **1**, 105 (2010).
- [16] F. Lechermann, N. Bernstein, I. I. Mazin, and R. Valentí, *Phys. Rev. Lett.* **121**, 106401 (2018).
- [17] S. A. Carter, T. F. Rosenbaum, M. Lu, H. M. Jaeger, P. Metcalf, J. M. Honig, and J. Spalek, *Phys. Rev. B* **49**, 7898 (1994).
- [18] F. Rodolakis, P. Hansmann, J.-P. Rueff, A. Toschi, M. W. Haverkort, G. Sangiovanni, A. Tanaka, T. Saha-Dasgupta, O. K. Andersen, K. Held, M. Sikora, I. Alliot, J.-P. Itié, F. Baudelet, P. Wzietek, P. Metcalf, and M. Marsi, *Phys. Rev. Lett.* **104**, 047401 (2010).
- [19] P. Hansmann, A. Toschi, G. Sangiovanni, T. Saha-Dasgupta, S. Lupi, M. Marsi, and K. Held, *Phys. Status Solidi B* **250**, 1251 (2013).
- [20] J. Feinleib and W. Paul, *Phys. Rev.* **155**, 841 (1967).
- [21] G. A. Thomas, D. H. Rapkine, S. A. Carter, A. J. Millis, T. F. Rosenbaum, P. Metcalf, and J. M. Honig, *Phys. Rev. Lett.* **73**, 1529 (1994).
- [22] J. S. Brockman, L. Gao, B. Hughes, C. T. Rettner, M. G. Samant, K. P. Roche, and S. S.P. Parkin, *Nat. Nanotechnol.* **9**, 453 (2014).
- [23] R. Baddour-Hadjean, A. Boudaoud, S. Bach, N. Emery, and J.-P. Pereira-Ramos, *Inorg. Chem.* **53**, 1764 (2014).
- [24] G. Xu, X. Wang, X. Chen, and L. Jiao, *RSC Adv.* **5**, 17782 (2015).
- [25] M. Foguel and R. Grajower, *J. Cryst. Growth* **11**, 280 (1971).
- [26] H. R. Rasouli, N. Mehmood, O. Çakıroğlu, and T. S. Kasirga, *Nanoscale* **11**, 7317 (2019).
- [27] See Supplemental Material at <https://link.aps.org/supplemental/10.1103/PhysRevB.100.161107> for experimental details, details of the crystal synthesis, comparison of Raman data with literature, AFM, SEM, additional optical images, XPS, WDS, and XRD characterization of the crystal.
- [28] M. Tachibana, *Beginner's Guide to Flux Crystal Growth* (Springer, Tokyo, 2017).
- [29] G. F. Schneider, V. E. Calado, H. Zandbergen, L. M. K. Vandersypen, and C. Dekker, *Nano Lett.* **10**, 1912 (2010).
- [30] A. Puthirath Balan, S. Radhakrishnan, C. F. Woellner, S. K. Sinha, L. Deng, C. D. L. Reyes, B. M. Rao, M. Paulose, R. Neupane, A. Apte, V. Kochat, R. Vajtai, A. R. Harutyunyan, C.-W. Chu, G. Costin, D. S. Galva, A. A. Martí, P. A. van Aken, O. K. Varghese, C. S. Tiwary, A. Malie Madom Ramaswamy Iyer, and P. M. Ajayan, *Nat. Nanotechnol.* **13**, 602 (2018).
- [31] A. Puthirath Balan, S. Radhakrishnan, R. Kumar, R. Neupane, S. K. Sinha, L. Deng, C. A. De Los Reyes, A. Apte, B. M. Rao, M. Paulose, R. Vajtai, C. W. Chu, G. Costin, A. A. Martí, O. K. Varghese, A. K. Singh, C. S. Tiwary, M. R. Anantharaman, and P. M. Ajayan, *Chem. Mater.* **30**, 5923 (2018).
- [32] E. Hryha, E. Rutqvist, and L. Nyborg, *Surf. Interface Anal.* **44**, 1022 (2012).
- [33] G. Silversmit, D. Depla, H. Poelman, G. B. Marin, and R. De Gryse, *J. Electron Spectrosc. Relat. Phenom.* **135**, 167 (2004).
- [34] G. A. Sawatzky and D. Post, *Phys. Rev. B* **20**, 1546 (1979).
- [35] H. Nohira, W. Tsai, W. Besling, E. Young, J. Petry, T. Conard, W. Vandervorst, S. De Gendt, M. Heyns, J. Maes, and M. Tuominen, *J. Non-Cryst. Solids* **303**, 83 (2002).
- [36] P. D. Dernier and M. Marezio, *Phys. Rev. B* **2**, 3771 (1970).
- [37] P. D. Dernier, *J. Phys. Chem. Solids* **31**, 2569 (1970).
- [38] M. I.B. Utama, F. J. Belarre, C. Magen, B. Peng, J. Arbiol, and Q. Xiong, *Nano Lett.* **12**, 2146 (2012).
- [39] B. S. Allimi, S. P. Alpay, C. K. Xie, B. O. Wells, J. I. Budnick, and D. M. Pease, *Appl. Phys. Lett.* **92**, 202105 (2008).
- [40] N. Kuroda and H. Y. Fan, *Phys. Rev. B* **16**, 5003 (1977).
- [41] C. Tatsuyama and H. Y. Fan, *Phys. Rev. B* **21**, 2977 (1980).
- [42] L. J. Eckert and R. C. Bradt, *J. Appl. Phys.* **44**, 3470 (1973).
- [43] R. Gaillac, P. Pullumbi, and F.-X. Coudert, *J. Phys.: Condens. Matter* **28**, 275201 (2016).
- [44] Y. Sato and S. I. Akimoto, *J. Appl. Phys.* **50**, 5285 (1979).
- [45] H. J. Zeiger, *Phys. Rev. B* **11**, 5132 (1975).
- [46] A. Okamoto, Y. Fujita, and C. Tatsuyama, *J. Phys. Soc. Japan* **52**, 312 (1983).
- [47] H. Guo, M. I. Khan, C. Cheng, W. Fan, C. Dames, J. Wu, and A. M. Minor, *Nat. Commun.* **5**, 4986 (2014).
- [48] H. Kuwamoto, H. V. Keer, J. E. Keem, S. A. Shivashankar, L. L. van Zandt, and J. M. Honig, *J. Phys. symposia* **37**, C4-35 (1976).
- [49] J. Wu, Q. Gu, B. S. Guiton, N. P. de Leon, L. Ouyang, and H. Park, *Nano Lett.* **6**, 2313 (2006).
- [50] H. Kuwamoto, J. M. Honig, and J. Appel, *Phys. Rev. B* **22**, 2626 (1980).
- [51] B. Widom, in *Phase Transitions and Critical Phenomena*, edited by C. Domb and M. S. Green (Academic, London, 1972).
- [52] J. Vučićević, H. Terletska, D. Tanasković, and V. Dobrosavljević, *Phys. Rev. B* **88**, 075143 (2013).
- [53] F. Gorelli, M. Santoro, T. Scopigno, M. Krisch, and G. Ruocco, *Phys. Rev. Lett.* **97**, 245702 (2006).
- [54] G. G. Simeoni, T. Bryk, F. A. Gorelli, M. Krisch, G. Ruocco, M. Santoro, and T. Scopigno, *Nat. Phys.* **6**, 503 (2010).
- [55] C. H. Ahn, J. M. Triscone, and J. Mannhart, *Nature (London)* **424**, 1015 (2003).
- [56] S. Dai, Z. Fei, Q. Ma, A. S. Rodin, M. Wagner, A. S. McLeod, M. K. Liu, W. Gannett, W. Regan, K. Watanabe, T. Taniguchi, M. Thiemens, G. Dominguez, A. H.C. Neto, A. Zettl, F. Keilmann, P. Jarillo-Herrero, M. M. Fogler, and D. N. Basov, *Science* **343**, 1125 (2014).
- [57] A. M. Dubrovkin, B. Qiang, H. N. S. Krishnamoorthy, N. I. Zheludev, and Q. J. Wang, *Nat. Commun.* **9**, 1762 (2018).
- [58] T. G. Folland, A. Fali, S. T. White, J. R. Matson, S. Liu, N. A. Aghamiri, J. H. Edgar, R. F. Haglund, Y. Abate, and J. D. Caldwell, *Nat. Commun.* **9**, 4371 (2018).